International Journal of Multiphase Flow 157 (2022) 104235

Contents lists available at ScienceDirect

International Journal of Multiphase Flow

journal homepage: www.elsevier.com/locate/ijmulflow

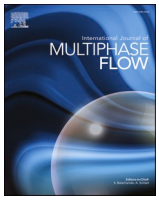

Droplet Impact on a Micro-structured Hydrophilic Surface: Maximum Spreading, Jetting, and Partial Rebound

Brooklyn Asai, Hua Tan *, Anayet Ullah Siddique

School of Engineering and Computer Science, Washington State University-Vancouver, 14204 NE Salmon Creek Ave., Vancouver, WA 98686, USA

A B S T R A C T

In this paper, we perform an experimental study of droplet impact on a partially wetting hydrophilic substrate composed of cylindrical micro-pillars. Water and glycerol are mixed at different ratios to primarily change liquid viscosity and keep surface tension approximately constant. We show that our microstructured hydrophilic surface can exhibit many of the same impact outcomes as hydrophobic surfaces including spreading, recoiling, jetting, and partial rebound. A regime map is constructed to convey the overall effects of the impact velocity and viscosity on the impact outcomes. Our data indicate that the maximum spreading factor β_{max} generally follows the power law with the Weber number We as $\beta_{max} \sim We^{0.25}$. However, the scaling relation of $\beta_{max} \sim We^{0.2}Re^{0.04}$ provides a better correlation for β_{max} because the viscous dissipative effect due to flow through the micro-pillars on the substrate becomes increasingly important for more viscous fluids. The rapid jet caused by the collapse of the air cavity in the recoil phase grows in a self-similar pattern. The relationship between the size of the top jet droplet and jet velocity is found to obey the same scaling law originally proposed for the bubble bursting jet. The partial rebound occurs only for low viscosity fluids with relatively high impact velocity. The size of the rebounding droplet emitted by the breakup of inertially stretched thick liquid thread in the partial rebound is found to be nearly independent of the impact velocity. The elapsed time between droplet impingement and partial rebound event scales with the capillary time.

1. Introduction

The impact of liquid droplets is ubiquitous and crucial in a myriad of natural and industrial processes, such as inkjet printing (Modak et al. 2020), pesticide spraying (Deng et al. 2021), additive manufacturing (Nemani et al. 2018), drug delivery (Baxter and Mitragotri 2006), and transport of aerosols (Lhuissier and Villermaux 2012), and many others. The outcomes of drop impact are quite diverse and dependent on a range of parameters, including properties of the liquid droplets (Yu et al. 2020; Zhao et al. 2017), drop size (Rioboo et al. 2001), particulates within the droplet (Lekshmi et al. 2020), wettability of the surface (Lin et al. 2018; Siddique et al. 2020; Yuan et al. 2021), surface features such as morphology (Courbin et al. 2006; Ding et al. 2020; Lv et al. 2016; Malla et al. 2017; Zhang et al. 2019), impact angle (Guo et al. 2020; Hao et al. 2019), temperature (Li et al. 2020; Prasad et al. 2022), and surrounding environment (Li et al. 2017). Within the last two decades, technology advancements have allowed researchers to more closely study the effects of surface on the outcomes of the droplet impact. High-speed photography (Thoroddsen et al. 2008; Versluis 2013) emerges as one of the most powerful tools that can provide very detailed and accurate information of various behaviors following droplet impact, including deposition, spreading, splashing, receding, jetting, breakup, rebounding, and shattering.

A lot of research efforts have been made to examine the underlying dynamics behind the wide range of outcomes following droplet impact on different types of substrates. One of the first instances recorded of these behaviors was the jet eruption following droplet impact on deep water pools observed by A. M. Worthington using a flash photograph technique more than a century ago (Worthington 1909), which is now often referred to as the Worthington jetting. In fact, jet ejection has also been observed in many other scenarios, such as the bursting of bubbles at the air-liquid interface (Gekle and Gordillo 2010; Ghabache et al. 2014; Li et al. 2019), pinch off of liquid droplets (Yamamoto et al. 2016), oscillating droplets (Thoroddsen et al. 2007b), and impinging droplets onto solid substrates (Chen et al. 2017; Zhao et al. 2020). Another behavior of interest that stems from droplet impact is the partial rebound (Mao et al. 1997; Parihar et al. 2021; Roy et al. 2019), which occurs when a large portion of the droplet breaks away and leaves part of the droplet remaining on the substrate. So far, a wide range of substrates have been employed to study droplet impact, such as bioinspired surfaces (Roy et al. 2019), superhydrophobic substrates (Tsai et al. 2009), and micro/nano-structured surfaces (Baek and Yong 2020; Bartolo et al. 2005; Laan et al. 2014; Lee et al. 2016; Li et al. 2013; Lin et al. 2018; Mao et al. 1997; Ukiwe and Kwok 2005; Wang et al. 2019).

Though much research on droplet impact has been focused on hydrophobic or superhydrophobic surfaces, less attention has been directed toward hydrophilic surfaces. In fact, hydrophilic surfaces are just as important as hydrophobic ones, as they are needed in many different applications ranging from biomedical devices to marine

* Corresponding author
E-mail address: hua.tan@wsu.edu (H. Tan).

https://doi.org/10.1016/j.ijmultiphaseflow.2022.104235
Received 10 June 2022; Received in revised form 16 August 2022; Accepted 23 August 2022
Available online 25 August 2022

engineering (Ahmad et al. 2018). Most existing studies on droplet hitting hydrophilic surfaces have been devoted to understanding the effects of surface wettability on the maximum spreading of droplet (Budakli 2021; Fedorchenko et al. 2005; Pasandideh-Fard et al. 1996; Sikalo et al. 2005; Ukiwe and Kwok 2005). In addition to simple deposition or splashing, droplet impact on smooth hydrophilic substrates can lead to some unexpected fascinating outcomes under certain conditions (e.g., impact velocity, surface wettability), such as rebound from the surface due to a thin air film formed between droplet and surface during impact (Chubynsky et al. 2020; Kolinski et al. 2014), ejection of the secondary droplet during the spreading (Ding et al. 2012) or retraction phase after impact (Liu et al. 2020). Recently, we have reported that a rapid jet can arise and then break up into one or multiple secondary droplets following the primary droplet impact on a micro-structured hydrophilic wafer surface at a certain range of the impact velocity (Siddique et al. 2020). We analyzed the dependence of the initial jet speed and jet dimensions prior to breakup (i.e., height and diameter) on the impact velocity and revealed that the jet is initialized by the inertial focusing of radial flow due to the collapse of an air cavity that forms at the center of the droplet during the retraction of the droplet. However, we did not investigate the transient aspect of the jet formation and breakup as well as the effect of microstructure of the substrate on the maximum spreading of the droplet. Additionally, the partial rebound phenomenon was just briefly presented in our previous work without any in-depth analysis.

Therefore, in this work we aim to uncover the fundamental dynamics of various impact outcomes following the impact of viscous droplets on the micro-pillared hydrophilic substrate, such as maximum spreading, high-speed jetting, satellite droplets ejected from the jet breakup, and partial rebound. Water-glycerol mixtures are used in our study to primarily vary liquid viscosity with small difference in the surface tension. The effects of the Weber number ($We = \rho U_i^2 D_i/\sigma$, where ρ, σ, U_i and D_i are the liquid density, surface tension, droplet impact velocity, and initial droplet diameter, respectively) and viscosity on the impact outcomes are quantified via high-speed video photography. A regime map of observed impact phenomena is presented and discussed for different impact velocities and fluid viscosities. We investigate the effects of the impact velocity and microstructure of the substrate on the maximum spreading of the impinging droplet. We find that during the recoil of the droplet, a rapid thin jet caused by the collapse of the air cavity grows in a self-similar pattern. The breakup of the jet is controlled by the balance between the capillary force and inertia. The relation between the satellite droplet size and the jet speed is quantified and analyzed. Finally, we study the partial rebound by analyzing the liquid profile prior to the pinch-off and quantifying the size of rebounding droplet.

2. Material and methods

2.1. Solution preparation and substrate

Solutions of a mixture of glycerol and deionized (DI) water were tested with a glycerol volume percentage ranging from 0-55%. Using a graduated cylinder, the calculated mass of DI water was first added, up to +/-0.001 g. Then the glycerol was added carefully by pipette until the total calculated fluid mass for both components was reached. The solution was then placed on a vortex mixer at 1275 RPM for approximately three minutes to homogenize the glycerol and DI water. The solutions used for our experiments consisted of DI water, 5, 10, 25, 35, 37.5, 40, 45, 50, and 55% glycerol. Properties for these solutions are listed in Table 1. A tensiometer and goniometer (Model 250 Ramé-Hart) were used to measure surface tension and contact angle, respectively, while a Brookfield viscometer was used to measure viscosity. The Ohnesorge number ($Oh = \mu/(\rho\sigma D_i)^{1/2}$) varies from 0.0023 to 0.023.

The substrate used for these experiments was a 4-inch (100) silicon wafer with various hydrophilic patterns etched into the surface. The wafer was cleaned using the standard wafer cleaning process, then rinsed with a large quantity of deionized (DI) water and dried under a stream of nitrogen gas. A silicon nitride (Si_3N_4) film was deposited on the Si wafer with plasma-enhanced chemical vapor deposition (PECVD) to be used as the etch mask for the anisotropic deep reactive ion etching (DRIE). The micropatterns were transferred from photomask to photoresist by a standard photolithography process. The top view of the fabricated surface – recorded by SEM (FEI Quanta 600 FEG) – is shown in Figure 1(a). The patterns created for our experiments consisted of cylindrical micropillars of varying height, diameter, and spacing. With this substrate preparation we were able to achieve 10 patterns per wafer, as shown in Figure 1(b). Characteristics of the pillars used in our experiments were diameter d = 52 μm, spacing s = 21 μm, and height h = 120 μm as shown in Figure 1(c). Contact angles were tested for most solutions on the wafer surfaces and were found to range from 43.6-51.4° as listed in Table 1, indicating that indeed the substrate was hydrophilic. It is worth noting that for the flat smooth substrate without micropillars, the contact angle for different solutions is nearly constant 37.4 ± 1.8°.

Table 1
Solution properties for all glycerol-water fluids used in experiments.

Solution (% G by volume)	Density ρ (kg/m^3)	Viscosity μ (mPa•s)	Surface Tension σ (mN/m)	Contact angle θ (o)	*Oh*
0 (DI water)	997	0.96	72	51.4	0.0023
5	1013	1.2	71.5	50.7	0.0027
10	1027	1.3	71	50.1	0.0029
25	1070	2.3	69.5	47.1	0.0051
35	1100	3.5	69	46.4	0.0077
37.5	1107	4.3	68.5	45.2	0.0095
40	1113	4.5	68	43.9	0.01
45	1127	5.8	67.5	43.6	0.012
50	1141	7.7	67	48.5	0.017
55	1155	10.5	66	49.4	0.023

2.2. Experimental setup

The experimental setup consists of a syringe pump, LED light source, high-speed camera, and precision motion stage as shown in Figure 2. A high-speed camera (Phantom Miro M310) with a Navitar 12X Zoom Lens was used to capture the impinging droplet. The camera was positioned horizontally in line with the motion stage on which the micro-structured wafer was placed. On the other side of the motion stage an LED light (AmScope LED-8WD) was positioned to provide backlighting for the droplet. Videos were taken at 8000-18000 fps with exposure times of 20 μs. Resulting pixel densities vary between 768 by 768 pixels and 512 by 320 pixels for these choices. Directly above the wafer surface was the dispensation setup that released the droplet of solution from the attached pipette tip. The syringe pump (New Era Pump Systems NE-1000) was used to electronically pump the syringe containing the glycerol/water solution through plastic tubing until a droplet was dispensed. To control the impact velocity, the height of the pipette tip was varied using a vertical motion stage (THOR Labs VAP10) connected to a 90-degree mounting bracket (THOR Labs AB90A) and metal breadboard (THOR Labs MB4).

For all experiments the substrate was mounted on a horizontal stage above which droplets were dispensed from the pipette tip. Liquid was delivered to the pipette using the programmable syringe-pump system until the pendant droplet detached from the tip and fell vertically towards the substrate. In all tests the diameter of the dispensed droplets was maintained at 2.7±0.02 mm, which was verified by profile view images that were recorded by the high-speed camera. Adjusting the drop release height led to a variation of the impact velocity from 0.49 to 1.17 m/s, with an uncertainty of ±0.01 m/s. Once in range of the camera, an auto-trigger was initiated to capture the subsequent events following droplet impact on the surface. These videos were then further processed by extracting images and analyzing them using an in-house developed MATLAB image processing code (MathWorks Inc.). Before and after each experiment, the micropillared surface was carefully cleaned with

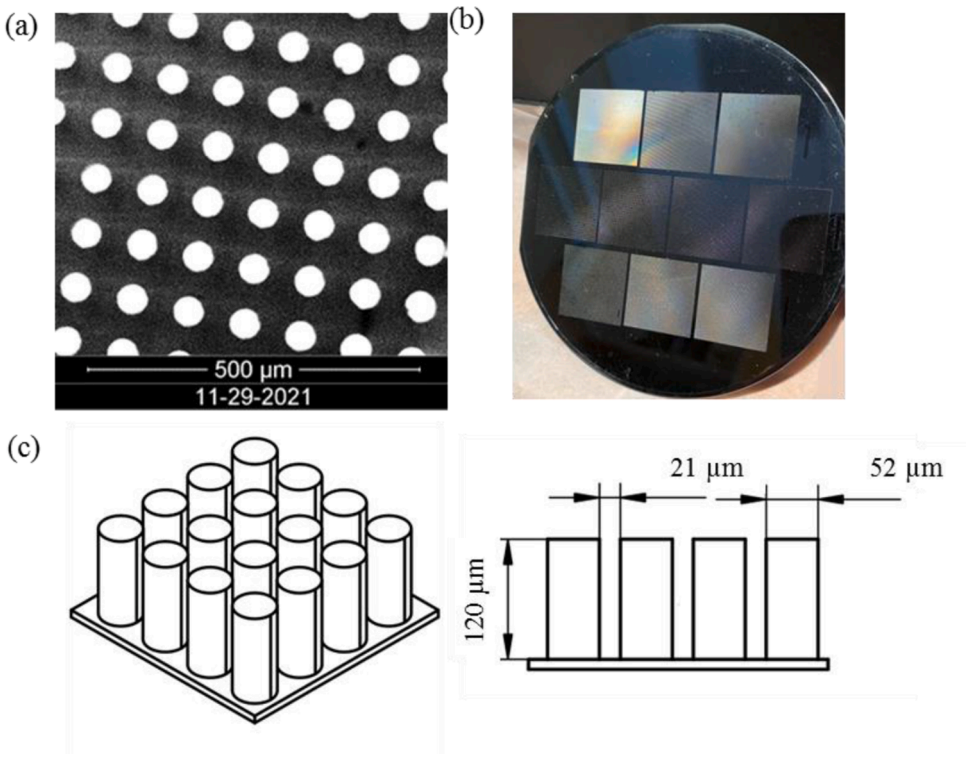

Figure 1. (a) SEM top-view of our substrate, (b) Image highlighting our specific pattern on the manufactured silicon wafer, (c) the schematic of our micro-pillared substrate including dimensions of micro-pillars.

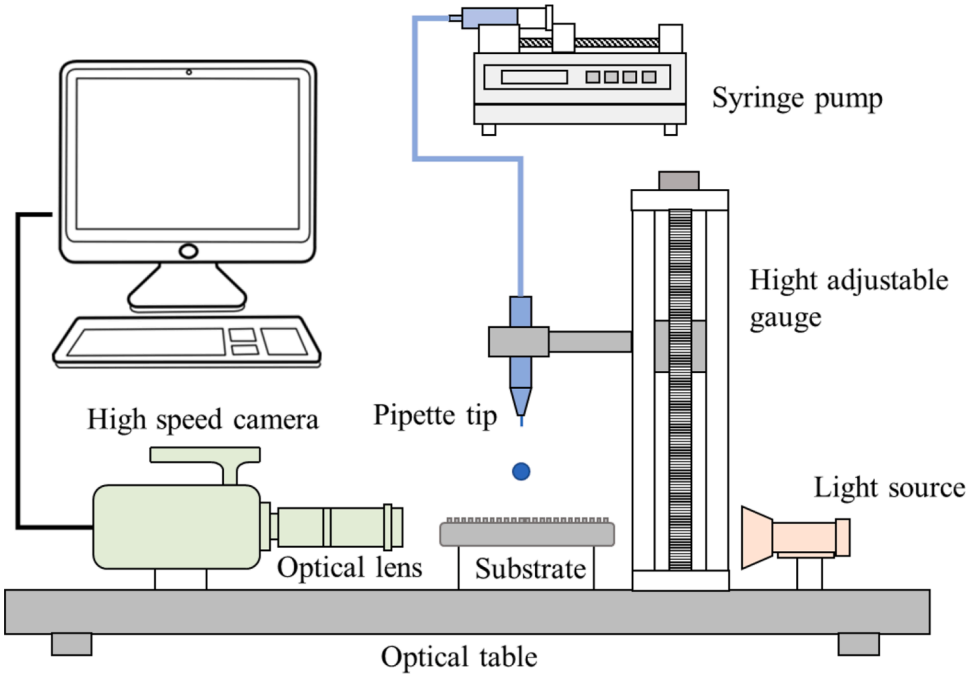

Figure 2. Schematic of experimental setup.

isopropanol, de-ionized water and allowed to dry out completely with the aid of a low temperature hot plate. Each data point gathered from a certain impact velocity and solution was repeated three times to ensure accuracy. Totally, we have run around 360 experiments for 10 test fluids.

3. Results and discussion

3.1. Impact outcomes

Various impact phenomena have been observed following droplet impact on our micro-pillared hydrophilic surface, such as spreading, jetting, jet breakup, and partial rebound. Figure 3 presents the snapshots

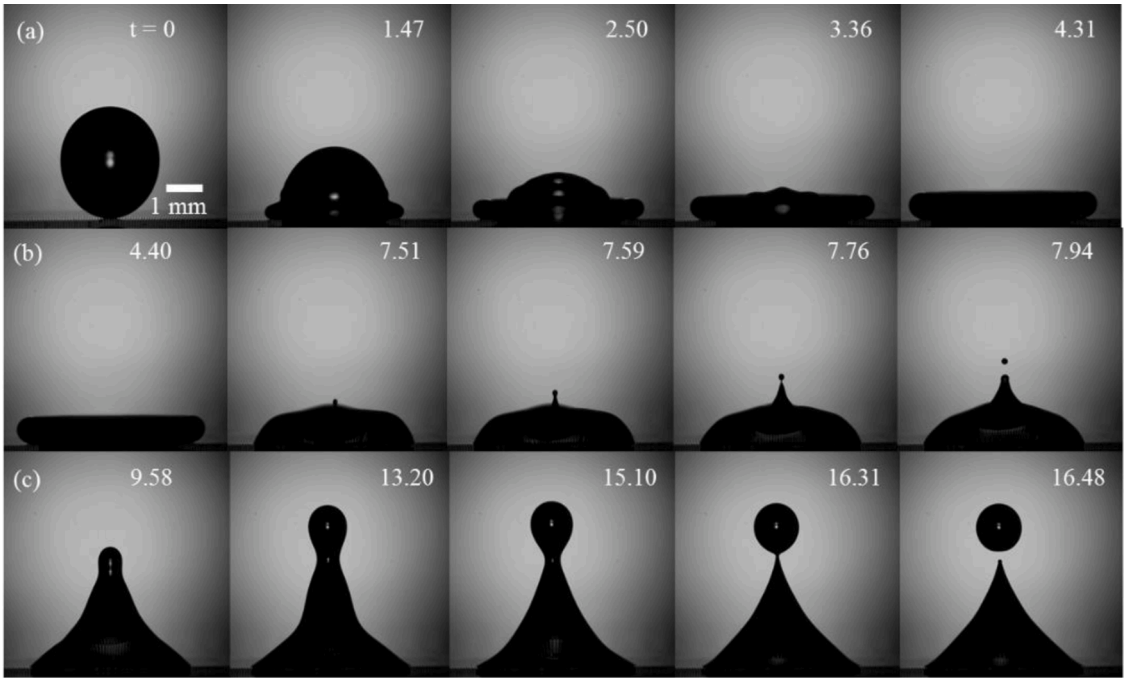

Figure 3. Image sequence for DI water where $U_i = 0.829$ m/s (We=26.1) with elapsed time in milliseconds from initial impact: (a) impact to maximum spreading, (b) jetting and single breakup, (c) partial rebound.

of the water droplet with impact velocity $U_i = 0.829$ m/s (*We*=26.1). This case involves all observed impact outcomes that develop at different post-impact times. Once the droplet impacts the substrate it goes through a spreading phase primarily driven by the inertia until it reaches a maximum diameter which is limited by surface tension and viscosity. The impact on the solid surface causes a capillary wave to propagate from the bottom to the top of the droplet along the droplet surface during spreading, resulting in a pyramidal structure of the droplet profile as shown in Figure 3(a). Such capillary wave is completely suppressed by viscous force for more viscous liquid ($\mu \geq 3.5$ mPa•s).

After maximum spreading, the droplet retracts radially due to surface tension, forming a lamella shape as shown in Figure 3(b). A thin jet can be seen to emerge from the center of the recoiling lamella at 7.51 ms. The speed of the jet tip reaches as high as 6.1 m/s at the moment it passes the recoiling rim. Similar jetting phenomenon has been well reported for droplet hitting a superhydrophobic substrate. Our previous study (Siddique et al. 2020) has shown that the high-speed jet observed for our micro-structured hydrophilic surface is caused by the inertial focusing of the radial flow due to the collapse of an air cavity formed at the center of lamella. As the jet stretches upward, the tip of the jet grows into a blob until it pinches-off to form a satellite droplet at 7.76 ms. The size of the satellite droplet is typically of tens of micrometers in diameter.

Following ejection of the jetting droplet, inertial and capillary forces continue to drive liquid upward, deforming the droplet into a thick stretched liquid column with a growing bulb on its top that eventually detaches as a large satellite droplet at 16.48 ms (as shown in Figure 3 (c)). The detached satellite droplet often moves up slowly while a large portion of the droplet remaining on the substrate, i.e., the partial rebound occurs. The satellite droplet produced in the partial rebound is usually of hundreds of micrometers in diameter.

In our study, we find the cavity-collapse driven jet observed in the recoil phase typically pinches off ejecting a single or multiple satellite droplets. When no jetting or partial rebound is found to occur, we have observed just simple deposition with post-impact oscillation. To understand how impact velocity and viscosity affect the impact dynamics, a regime map of impact outcomes is created in Figure 4 according to *We* and *Oh* for the experiments performed. There are four distinct regimes in the droplet impact regime map including (1) simple deposition, (2) jet with a single droplet ejection, (3) jet with multiple droplet ejections, and (4) the partial rebound regime. In the regime map, 'JS' corresponds to cases of single satellite droplet ejection following jetting, 'JM' for multiple satellite droplets ejected after jetting, 'PR' for partial rebound cases, and 'N' for cases where only deposition occurs. For each test fluid (corresponding to a specific *Oh*), different impact velocities (i.e., *We*) were used in the experiments, so the impact outcomes for a specific *We* were labeled according to these four categories to create the regime map. If multiple outcomes are observed for a single impact event (e.g., the case of Figure 3), these markers to represent different outcomes will overlap at the same location in Figure 4.

No jet is observed for viscous solutions with $\mu > 10.5$ mPa•s ($Oh > 0.023$). In such cases the inertial-capillary waves driving the motion to form the jet during recoil are damped in a similar manner as are jets created by viscous bursting bubbles. The partial rebound is only observed for less viscous solutions with $\mu \leq 2.3$ mPa•s ($Oh \leq 0.0051$). Both jetting and partial rebound are observed to occur in a certain range of *We*.

We need to mention that there are a couple of reasons why the current regime map Figure 4 looks moderately different than the regime map in the previous paper (Siddique et al. 2020). First, we have improved our droplet dispensation system to minimize the oscillation of the impacting droplet induced by the detachment of the droplet from the pipette needle. Our previous experiments with low-viscosity fluids have shown that such spurious oscillations resulted in large variation of the jet dynamics (i.e., the repeatability issue), precluding us from doing reliable analysis of jetting dynamics for low-viscosity fluids. With the improved dispensation system, we obtained more repeatable data for these low-viscosity fluids. To be consistent we have re-run the droplet impact experiments of high-viscosity fluids as well. Second, our old regime map did not include the PR because we did not do any rigorous analysis for the PR event.

For a given liquid, jetting only arises for a certain range of *We* in a similar manner to previous studies involving hydrophobic substrates

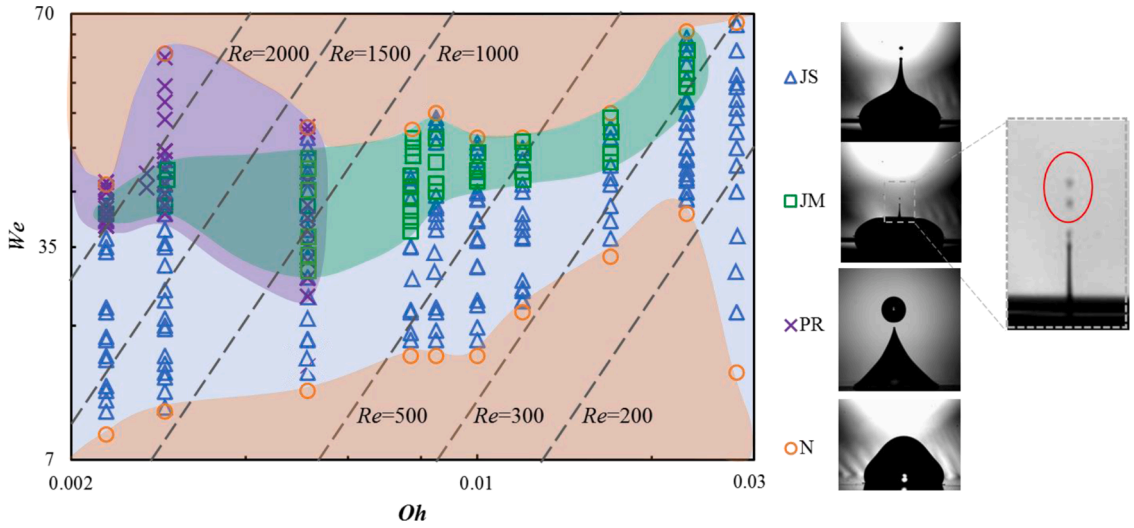

Figure 4. Regime map of impact outcomes for all solutions arranged by Weber and Ohnesorge numbers.

(Bartolo et al. 2006; Chen et al. 2017; Guo et al. 2020; Lin et al. 2018; Roy et al. 2019; Zhao et al. 2017). The lower bound of the *We* range above which the jet appears is higher for our micro-structured hydrophilic substrate than those reported in previous studies using hydrophobic surfaces. With further increases in *We*, the jet generally becomes thinner, shorter, and faster for the same liquid. When *We* exceeds the upper bound, the no jet regime is again observed. The jet experiences only one droplet ejection at low *We*, but multiple droplet ejections at high *We*, as identified in the two droplet-ejection regimes of the map. The emitted droplet can move up to 7.1 m/s. In both regimes, the lower and upper bounds of the jetting *We* range increase with increasing viscosity.

Partial rebound only occurs for lower viscosity fluids ($\mu \leq 2.3$ mPa•s) at relatively high impact velocities (0.805 m/s $\leq U_i \leq$ 1.17 m/s). There is an overlap between partial rebound and jetting regimes for low viscosity solutions, as shown in Figure 4. Partial rebound usually follows the initial breakup of the jet as shown in Figure 3, however it can occur without initial jetting prior to it. After the initial breakup emitting one or more small satellite droplets, the jet keeps growing into a thick and elongated liquid column due to the inertia, while the contact line is pinned by the hydrophilic micro-pillars on the substrate. After a certain height necking develops and eventually ruptures, pinching off a large satellite droplet of order of a few hundred micrometers up to around 1 mm in diameter. Further discussion concerning the partial rebound is reserved for Section 3.4.

It is worth mentioning that we also conducted droplet impact on the smooth wafer surface and did not observe any jetting or partial rebound phenomena discussed here. Therefore, the micro-pillars on the substrate plays a vital role in producing the jet and partial rebound. Additionally, we did not observe the complete droplet rebound from our micro-structured surface that often occurs for the droplet impact on a hydrophobic surface with suitable conditions.

Finally, for some of the impact velocities within the regime map, we observe multiple of the discussed phenomena, or compound outcomes, occurring for a singular droplet impingement. Some examples of this can be the appearance of multiple jetting where multiple, smaller satellite drops are followed by a singular, larger breakup, single jet breakup followed by partial rebound, or multiple satellite droplets followed by partial rebound. The following sections will discuss in more detail to characterize the outcomes of maximum spreading, jetting, and partial rebound.

3.2. Maximum spreading

The maximum spreading factor $\beta_{max}=D_{max}/D_i$ (where D_{max} is the maximum diameter when droplet spreads most) during the impact process is now discussed. Various simplified equations based on semi-empirical or theoretical models have been proposed to predict β_{max} for droplet impact on solid surfaces using the Reynolds number, Weber number, contact angle, and roughness (Baek and Yong 2020; Bartolo et al. 2005; Budakli 2021; Fedorchenko et al. 2005; Laan et al. 2014; Lin et al. 2018; Pasandideh-Fard et al. 1996; Ukiwe and Kwok 2005). If viscous dissipation is negligible, one could expect full conversion from kinetic energy to surface energy and hence obtain the scaling law $\beta_{max} \sim We^{0.5}$ by energy conservation. Under the similar capillary dominant condition, Clanet et al. (Clanet et al. 2004) proposed a different scaling law $\beta_{max} \sim We^{0.25}$ using momentum conservation. If instead the viscous dissipation plays a dominant role during the spreading, the scaling law $\beta_{max} \sim Re^{0.2}$ (Fedorchenko et al. 2005)or $Re^{0.25}$ (Pasandideh-Fard et al. 1996) is then expected.

Overall, we find these scaling laws utilizing *We* give us the best fit for our data. Figure 5 plots our experimental β_{max} against *We* for all tested fluids. Our data are well fitted with the scaling law of $\beta_{max} \sim We^{0.25}$, which is in a good agreement with Clanet et al.'s work(Clanet et al. 2004). It implies that droplet spreading in our experiments is also dominated by capillary force. However, we do notice that the trend of β_{max} vs. *We* for the most viscous fluid 55%G (μ= 10.5 mPa•s) tends to follow the scaling law behavior $\beta_{max} \sim We^{0.2}$. While this is not a large difference, it does raise the question whether the viscosity, in the form of including *Re* in scaling, can be completely ignored or not.

To address the viscous effect observed in Figure 5, we rescale β_{max} and *We* using $Re^{-0.2}$ and $Re^{-0.8}$, respectively(Clanet et al. 2004). Dimensionless group $\beta_{max}Re^{-0.2}$ can be viewed as the experimentally measured β_{max} normalized by the theoretically predicted $\beta_{max} \sim Re^{0.2}$ for the viscous regime (Fedorchenko et al. 2005), whereas $P=WeRe^{-0.8}$ is defined as the impact number by Clanet et al. (Clanet et al. 2004). Figure 6 plots $\beta_{max} Re^{-0.2}$ as a function of *P* with log-log scale. Clearly, all our data collapse quite neatly into a line with a scaling exponent of 0.2, i.e., $\beta_{max} \sim We^{0.2}Re^{0.04}$. The impact number *P* is less than 1 even for the most viscous solution, therefore we can determine that our solutions, while over a relatively large range of viscosities, lie in the capillary regime. However, the viscous dissipation during spreading cannot be completely ignored. Next, we carry out the energy balance analysis to understand the role played by the viscous dissipation during the droplet spreading over our microstructured substrate.

The value of β_{max} predicted by the scaling law of $\beta_{max} \sim We^{0.25}$ or $We^{0.2}Re^{0.04}$ from our experimental data is less than that calculated from the scaling law of $\beta_{max} \sim We^{0.5}$ which is obtained by assuming full conversion from kinetic energy *KE* to surface energy *SE*, suggesting that *KE* is not fully transformed to *SE* during spreading. Clanet et al. (Clanet

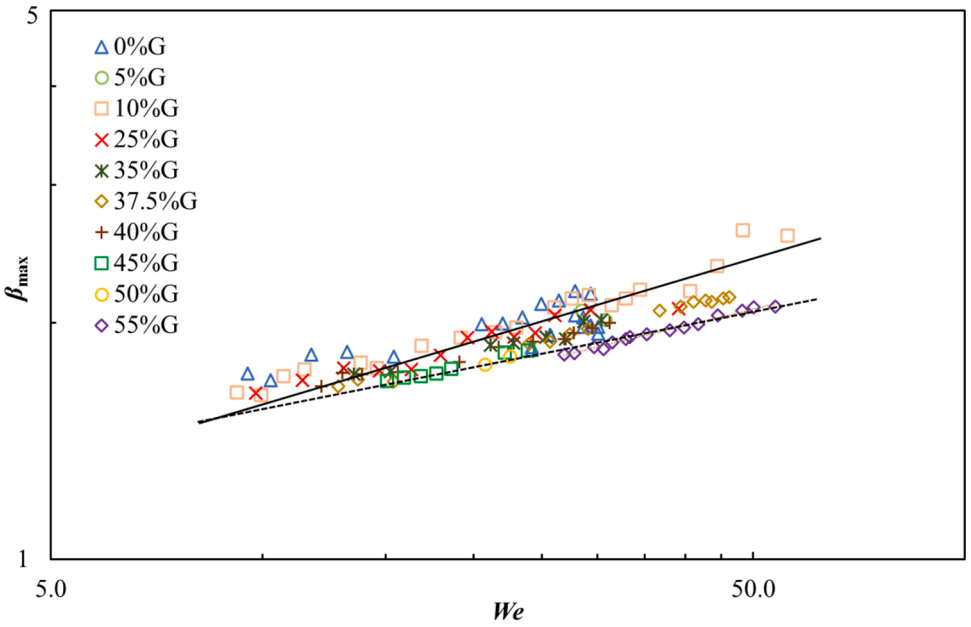

Figure 5. Log-log plot of maximum spreading factor β_{max} against We for all solutions. The solid line is $\beta_{max} \sim We^{0.25}$ fitted from our experimental data, while the dashed line is $\beta_{max} \sim We^{0.2}$ fitted from the data of most viscous fluid 55%G (μ =10.5 mPa•s).

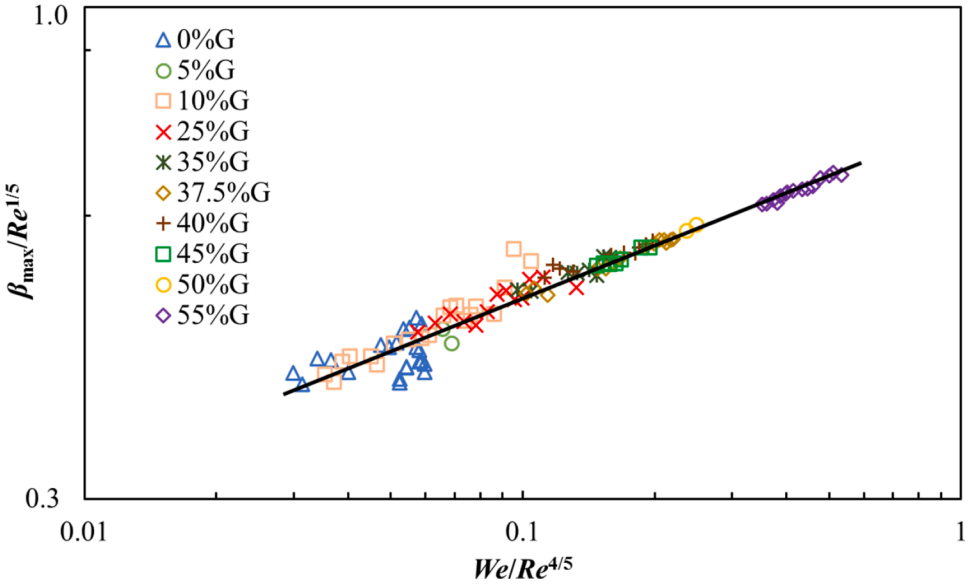

Figure 6. Log-log plot of $\beta_{max}Re^{-0.2}$ versus the impact number $P=WeRe^{-0.8}$. The solid line is $\beta_{max}Re^{-0.2} \sim P^{0.2}$ fitted from our experimental data.

et al. 2004) attributed the missing energy to portion of *KE* remaining in the droplet at the maximum spreading due to the existence of the vortical flow inside the lamella rim. However, our previous numerical study (Tan 2017) has shown that for partially wetting smooth surface such remanent *KE* stored in the lamella rim at the maximum spreading is often small and less than 5% of the initial *KE*. Instead, we believe that for our microtextured hydrophilic substrate the dissipation of initial *KE* due to viscous friction of fluid passing through the arrays of micropillars plays a nonnegligible role during spreading(Li et al. 2013). Such dissipative energy E_d can be estimated using the contact line movement(Baek and Yong 2020), i. e., $E_d = \sigma Ca D_{max}^2$ (where $Ca = \mu U_{cl}/\sigma$ is the capillary number based on the velocity U_{cl} of the contact line). Our experimental data indicate that *Ca* approximately follows a power law with *We* as $Ca \sim We^{0.5}$, which is also in good agreement with the definition of *Ca*. Considering the energy conservation from the initial impact to the maximum spreading, we have $KE_i + SE_i = E_d + SE_{max}$ with scaling relations including $KE_i \sim \rho U_i^2 D_i^3$, $SE_i \sim \sigma D_i^2$, $E_d \sim \sigma We^{0.5} D_{max}^2$, and $SE_{max} \sim \sigma D_{max}^2$. Nondimensionalizing the energy balance equation leads to $We+1\sim(We^{0.5}+1)\ \beta_{max}^2$. Since $We >> 1$ in our experiments, we can obtain the same scaling law of $\beta_{max} \sim We^{0.25}$ as proposed by Clanet et al. (Clanet et al. 2004). Our energy analysis indicates that portion of the initial *KE* is converted into the viscous dissipative energy due to fluid flow between micropillars on our substrate. As a result, β_{max} scales with $We^{0.25}$ instead of $We^{0.5}$. Finally, we plot the normalized dissipative energy Ed/SE_i against the impact number *P* in Figure 7. Surprisingly, all data points in the log-log scale collapse nearly into a line with a slope of 1.2, i.e., $Ed/SE_i \sim We^{1.2}Re^{0.96}$. It is clear from Figure 7 that for relatively high viscosity solutions (> 45%G, $\mu \geq$ 5.8 mPa•s), dissipative energy E_d due to viscous friction between the liquid and the ensemble of micropillars is relatively large and hence not negligible during spreading.

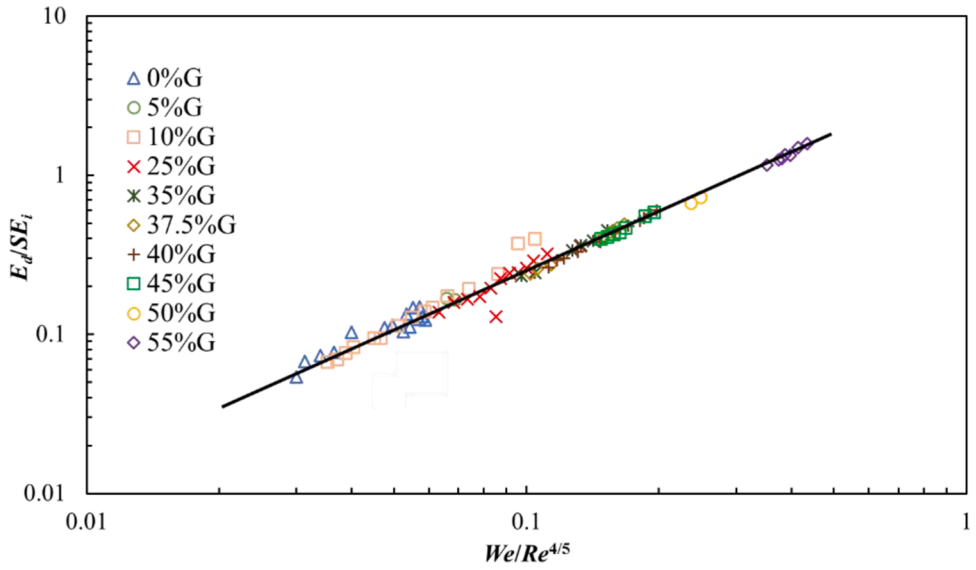

Figure 7. Log-log plot of normalized viscous dissipation E_d/SE_i versus the impact number $P=WeRe^{-0.8}$. The solid line is $E_d/SE_i \sim P^{1.2}$ fitted from our experimental data.

3.3. Jet formation and breakup

Another outcome following droplet impact on our microtextured hydrophilic substrate is the evolution of a high-speed jet, which was found to occur at Weber numbers between 9.2-67.1 for less viscous solutions with $Oh \leq 0.023$. Jetting was not observed for impact velocity $U_i < 0.51$ or > 1.07 m/s. The process of jetting always occurs in the recoil phase as shown in Figure 3(b). Our previous study (Siddique et al. 2020) has revealed the jets are caused by inertial focusing of radial flow at the point of the air cavity collapse. After the droplet reaches the maximum extension, it undergoes a recoiling phase in which a cylindrical air cavity forms in the center of the droplet. While recoiling, the air cavity shrinks in diameter as capillary and inertial forces pull the fluid fronts closer. Eventually the fluid fronts collide in the radial direction, resulting in a singularity at the center of the droplet which produces a high-speed vertical jet many times faster than the initial impact velocity (Bartolo et al. 2006; Zeff et al. 2000). As the jet continues to grow, a bulbous end forms at the tip of the jet and necking occurs due to surface tension forces which eventually causes the breakup of the jet and ejection of one or multiple satellite droplets. In this work, the objective is to investigate the evolution of jet profile and breakup as well as the size of emitted satellite droplets.

Jets induced by collapsing free-surface flows have also been observed in many other scenarios (Chen et al. 2017; Gekle and Gordillo 2010; Ghabache et al. 2014; Li et al. 2019; Rao et al. 2018; Thoroddsen et al. 2007b; Yamamoto et al. 2016; Zhao et al. 2020). For example, the burst of an air bubble at the free surface of a liquid generates a series of capillary waves propagating and converging at the bottom of the cavity to gives rise to the jet. The bubble bursting jet has been shown to exhibit self-similar dynamics (Brasz et al. 2018; Gañán-Calvo 2017; Lai et al. 2018). To see if the jet growth in our experiments also follows a self-similar pattern, we adopt the similar scaling approach for nondimensionalizing the evolution of jet profiles as these studies(Brasz et al. 2018; Gañán-Calvo 2017; Lai et al. 2018). The key dimensions of the jet profile including the jet height z_{jet}, radius of the jet r_{jet}, and the neck diameter n_d (as shown in Figure 8) are normalized by the capillary length $l_c = (\sigma/\rho g)^{0.5}$. The dimensionless time τ for describing the jet growth is given by $\tau = (t\text{-}t_c)/\tau_c$, with the current time t, the time of cavity collapse t_c, and the capillary time $\tau_c = (\rho D_i^3/\sigma)^{0.5}$. A scaling factor α can be derived using the power-law fit of the data of dimensionless jet geometric parameters vs. dimensionless length, i.e, $z_{jet}/l_c \sim \tau^{\alpha}$ or $r_{jet}/l_c \sim \tau^{\alpha}$. The

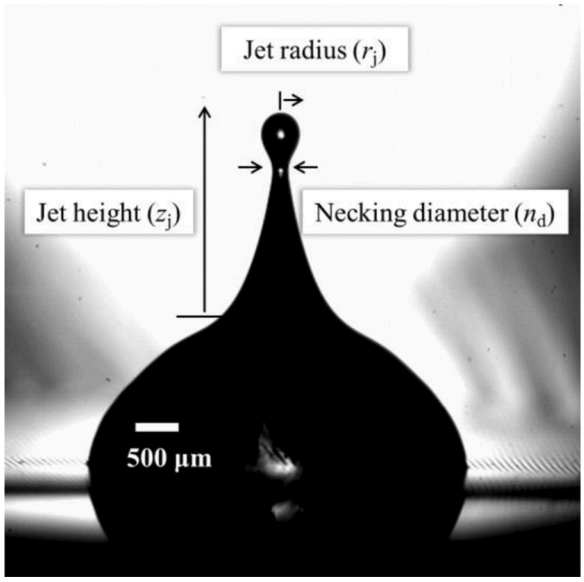

Figure 8. Key jet dimensions are extracted using the captured high-speed images (the image of 10%G solution at We = 13.8).

average scaling exponent α among all jetting cases for the height and radius of the jet was found to be ~ 0.94 and ~ 0.22 respectively, which are different than the universal scaling factor of 2/3 found in jets induced by bubble busting (Brasz et al. 2018; Gañán-Calvo 2017; Lai et al. 2018). Once α is obtained, the evolution of jet profiles over time are rescaled to check the self-similar behavior of the jet growth by using the shape factor $r = (\sigma/\rho)^{1/3}(t\text{-}t_c)^{\alpha}$. One example, as shown in Figure 9, plots the superimposed jet profiles for different times before and after rescaling for the 50%G solution at $We = 22.6$. We can clearly find that the jet profiles at different times collapse into one approximate master curve, thus indicating that the jet does indeed exhibit self-similar growth over time. It is worth noting that the scaling exponent α for the jet profile in our study is different for the jet height and radius, suggesting that any self-similar solution for the evolution of jet profile will require two different length scales (Thoroddsen et al. 2007a).

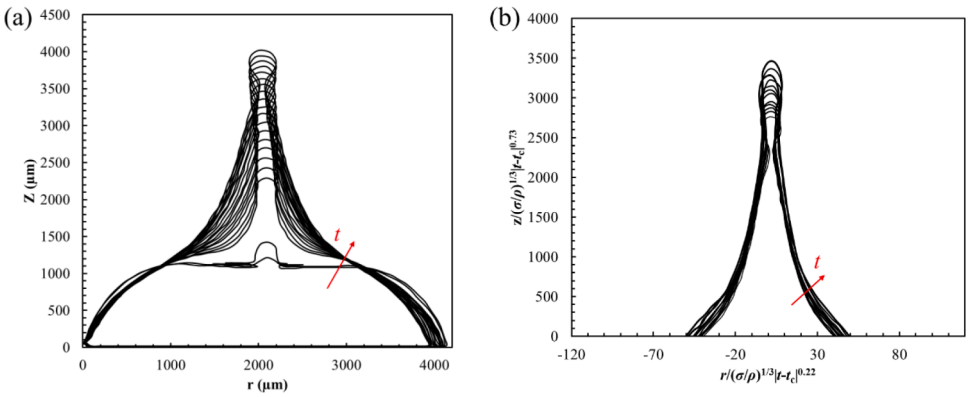

Figure 9. (a) Time evolution of the dimensional jet profile for a 50%G solution at We = 22.6 (Time interval is 0.091 ms); (b) The dimensionless jet profiles rescaled using the shape factor $(\sigma/\rho)^{1/3}(t\text{-}t_c)^{\alpha}$, where the scaling factor α is 0.73 and 0.22 for the jet radius and height, respectively.

The jet observed in our experiments is stretched inertially with the tip gradually growing into a bulb. Because the bulbous tip moves slower than the fluid in the thread located just behind it, the liquid can flow into the tip and increase its size. As the bulbous tip is growing, necking is found to occur where the jet joins the bulb due to the surface tension, eventually resulting in the rupture of the jet. The breakup of the jet always takes place at the jet tip detaching one droplet at a time, which is identical to 'end pinch-off' phenomena observed in ejection of satellite droplets due to bursting bubbles[Brasz et al. 2018; Gañán-Calvo 2017; Lai et al. 2018]. In this case, the capillary force opposed to the motion of the jet tip is the major source of perturbations leading to the pinch-off. The diameter of the neck reduces on the capillary time scale $\tau_j = (\rho r_{jet}^3/\sigma)^{0.5}$ based on the jet radius r_{jet}. As r_{jet} in our experiments varies from tens of μm to hundreds of μm, the breakup time is on the sub-millisecond scale. To find the scaling behavior of the necking process, we plot the dimensionless neck diameter n_d/l_c against the dimensionless time to the pinching $\tau = (t_b\text{-}t)/\tau_j$ (where t_b is the time at the moment of the jet pinch-off) in Figure 10. For all solutions, the data for n_d/l_c vs. τ generally collapse into a power law $n_d/l_c \sim \tau^{\alpha}$ with a scaling exponent of $\alpha = 0.63$ that is very close to 2/3, suggesting that the pinch-off process is dominated by the capillary and inertial forces, i.e., inviscid pinch-off [Eggers and Villermaux 2008].

Although the viscous force plays a little role in the scaling behavior of the neck diameter for all tested solutions, however we do find it has more influence on the evolution of the neck shape during the pinching process. In the water case, the neck of the jet is a cone-shaped thread connected to the bulbous tip at the incipience of the pinch-off, as shown in Figure 11a. However, for the most viscous solution 55%G (μ = 10.5 mPa•s), there exists a very thin (only a few μm thick) microthread between the nearly spherical jet tip and the primary thread of the cone structure prior to the breakup, as shown in Figure 11b. Such thin microthread connected to the primary thread is often observed to occur in the jet pinch-off experiments involving high viscosity fluids[Eggers and Villermaux 2008]. It is also noticeable that the cone-shaped thread behind the pinching location becomes slenderer for less viscous fluids.

The jet observed in our experiments is initialized by the cavity collapse [Siddique et al. 2020], which also causes the jet formation in bubble bursting. Therefore, we are wondering if the scaling laws established for the top droplet size and speed associated with the bubble bursting jet can be applied to our study. Gañán-Calvo [Gañán-Calvo 2017] proposed the scaling relationships for the size of ejected satellite droplet and the jet speed as $R_d/l_\mu \sim V_j/V_\mu^{-5/3}$ with visco-capillary length $l_\mu = \mu^2/\rho g$ and

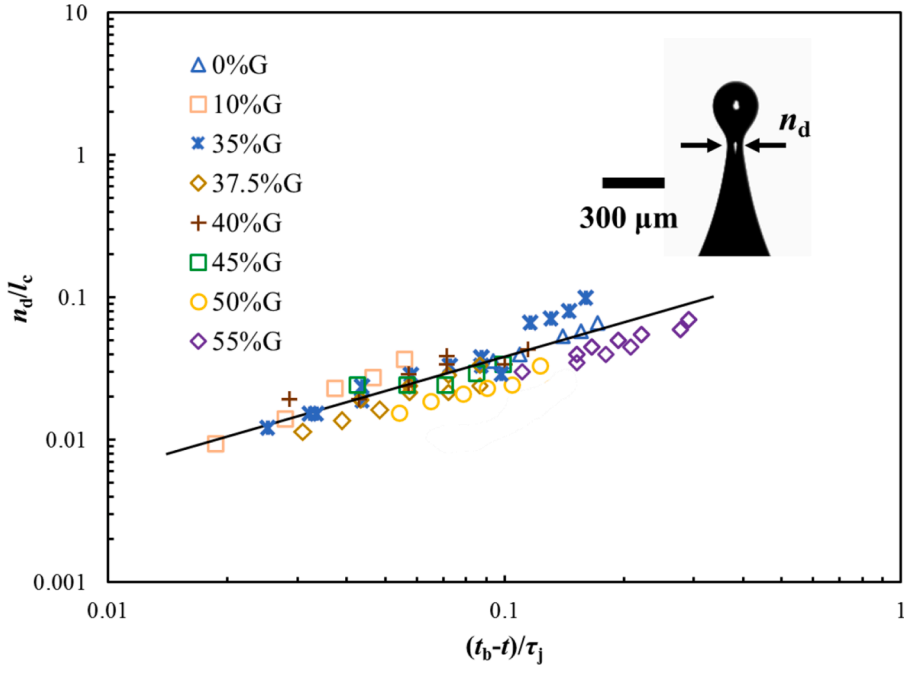

Figure 10. Dimensionless neck radius n_d/l_c as a function of the dimensionless time $\tau = (t_b\text{-}t)/\tau_j$. The solid line is $n_d/l_c \sim \tau^{0.63}$ fitted from experimental data.

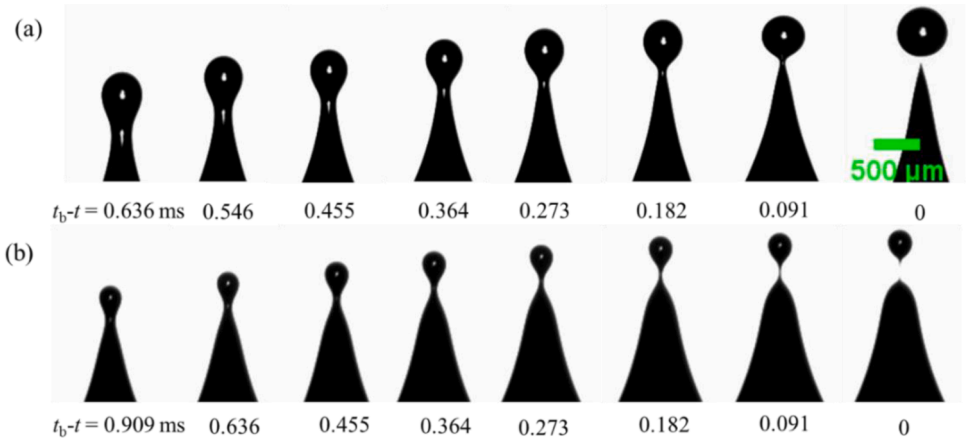

Figure 11. Necking process for two different fluids: (a) DI water at We = 10, (b) 55%G solution at We = 26.9.

visco-capillary velocity $V_\mu = \sigma/\mu$. We plot our measured data of R_d/l_μ in the function of V_j/V_μ in Figure 12, which clearly shows that the data points generally collapse into the scaling relation of $R_d/l_\mu \sim V_j/V_\mu{}^{-5/3}$, as suggested by Gañán-Calvo [Gañán-Calvo 2017]. Figure 12 also includes the data of low-viscosity fluids that were absent in our previous work due to the repeatability issue of these fluids caused by spurious oscillations of the impacting droplet induced by the detachment of the droplet from the pipette needle. Therefore, we can conclude that the scaling laws of the emitted droplet size and the jet speed proposed for the bubble bursting jet are generally applicable for the jet induced by the cavity collapse in the droplet impact.

3.4. Partial rebound

Partial rebound is found to occur from our experiments in the regions of relatively low viscosity and under a short range of impact velocities. More specifically, solutions of $\leq$ 25% glycerol ($Oh \leq 0.0051$) with impact velocities ranging from 0.805-0.970m/s were found to exhibit this outcome. A typical process of the partial rebound following the initialization of the thin jet is shown in Figure 3(c). After the breakup of cavity-collapse induced jet during the recoil phase, the inertia force continues to stretch the jet vertically and deforms it into a thick and elongated liquid column. After exceeding certain height, the liquid column becomes unstable because of the Rayleigh-Plateau instability and finally ruptures, pinching off a large top droplet with the base portion still sticked to the substrate. The emitted top droplet usually moves up at a very low speed and falls back very soon due to gravity. It then collides with the base droplet and continues rebounding, never coalescing with the base droplet in most cases.

Substrate characteristics play an important role in initiating the partial rebound. Since our surface is microtextured and hydrophilic, once the contact line becomes pinned by the micro-pillars on the substrate during retraction, the flow near the substrate begins to aid in the separation of the rebounding droplet. As the droplet grows into the column of liquid, the flow in the stretched column is being pulled in two opposite directions, i.e., the pulling of the lower portion to the wetted surface and the opposing upward inertial force of the flow within the separating portion of the droplet [Driessen et al. 2013; Ghigliotti et al. 2013].

Figure 13 shows the snapshots of the droplet profile of different solutions at different *We* immediately prior to the breakup in the partial rebound regime. We find that for a given solution the impact velocity has a minor effect on the droplet profile and size of the satellite droplet. It is noticeable that the droplet shapes before the pinch-off can be generally divided into two groups. For DI water and 25%G solution, the droplet roughly takes on a sphere and cone shape just before breakup, whereas for 5%G and 10%G solutions, a more complicated shape exists

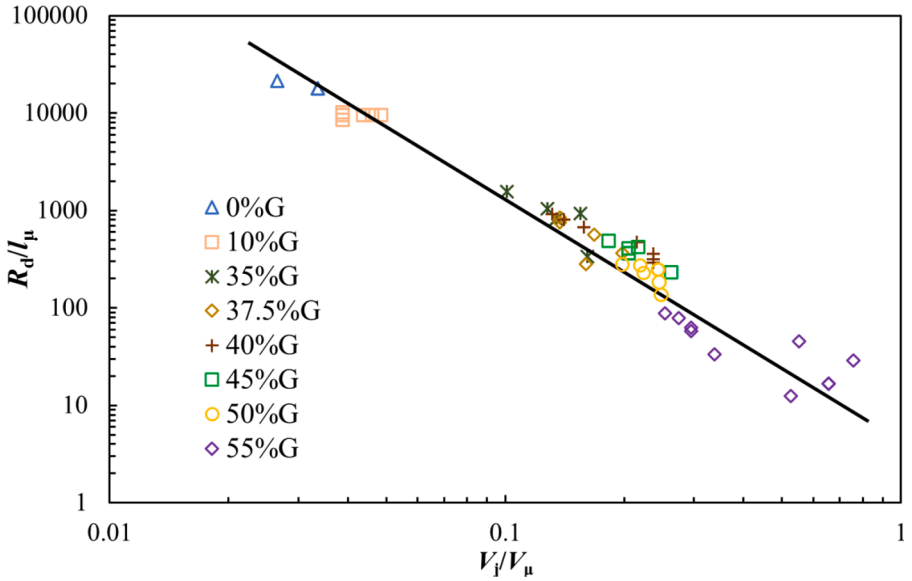

Figure 12. Plot of dimensionless ejected top droplet radius R_d/l_μ as a function of dimensionless jet velocity V_j/V_μ with the solid line representing the power law of $R_d/l_\mu \sim V_j/V_\mu{}^{-5/3}$.

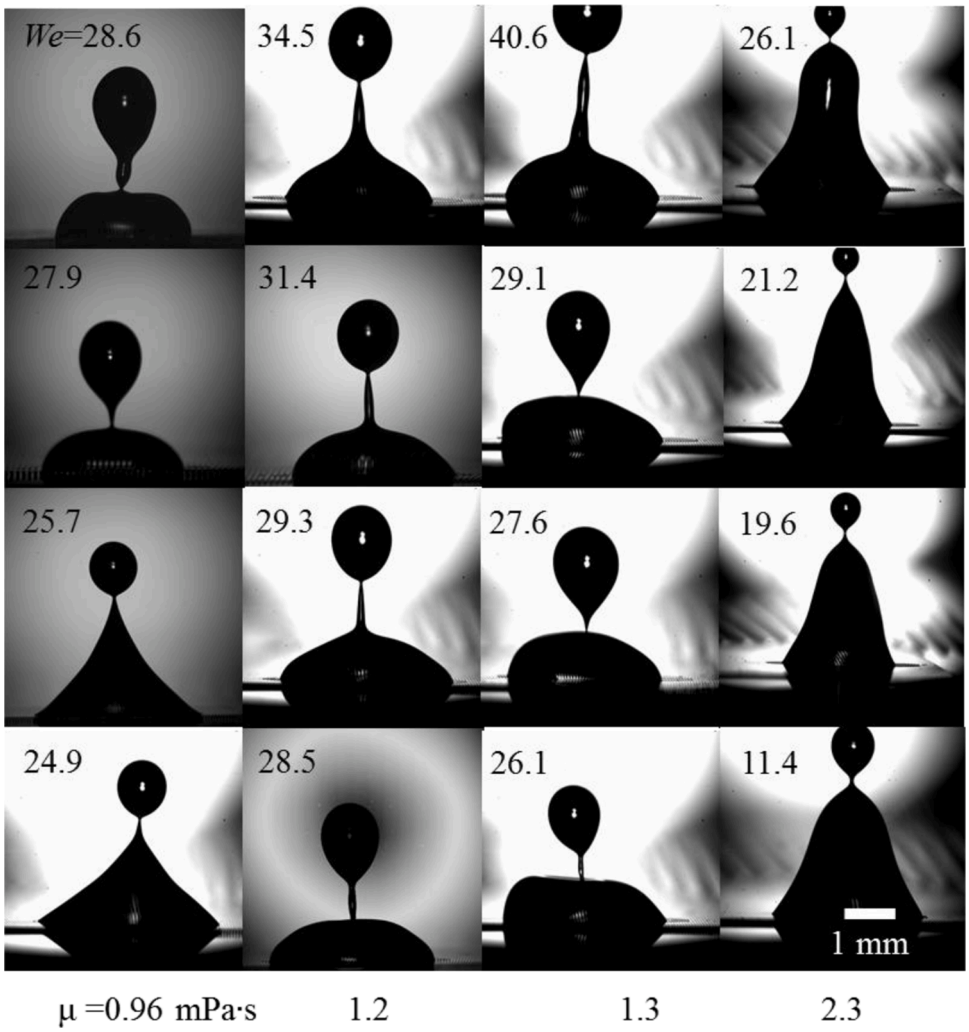

Figure 13. Images of the droplet shape just before breakup in the partial rebound regime for impacting droplet of specific μ and We.

that can generally be broken down into a cone, spherical cap, and sphere shape. Figure 14 shows the time evolution of the droplet profile for the two types. In the case of DI water (Figure 14(a)), the column of liquid pinches off at one location, producing a single large satellite droplet. However, in the case of 10%G solution (Figure 14(b)), as the capillary wave travels along the droplet surface, the pinching occurs at multiple locations in the stretched liquid column, leading to the formation of one primary satellite droplet and another much smaller one in the partial rebound.

One interesting characteristic observed from the partially rebounded top droplets in Figure 13 is an approximately constant droplet diameter independent of *We*. To quantify the effect of the impact velocity on the

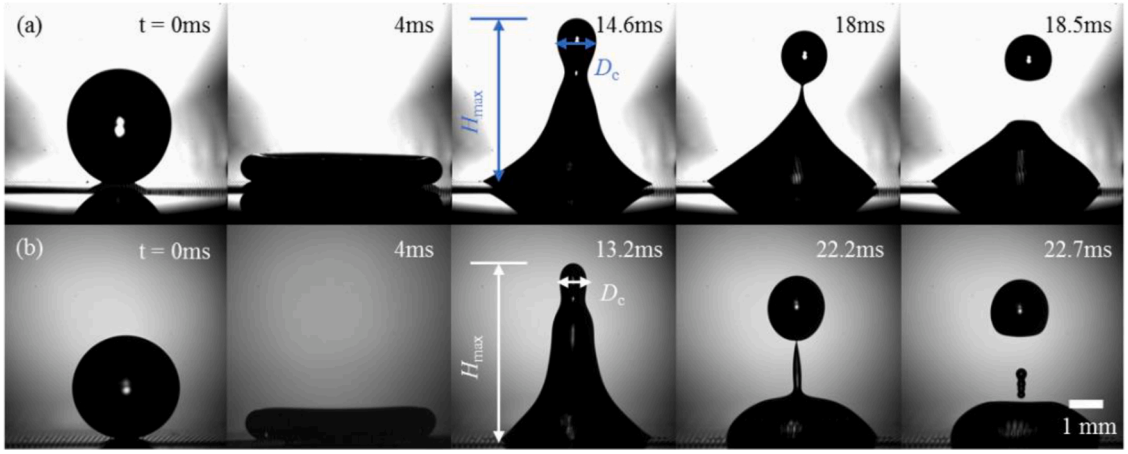

Figure 14. Evolution of two types of the droplet profiles in the partial rebound: (a) Cone and sphere shape for DI water at We = 24.9; (b) Spherical cap, small cone, and sphere shapes formed by 10%G solution at We = 31.4.

size of emitted satellite droplet during entire process of the droplet impact, we plot the ratio of the satellite droplet volume V_s to the initial droplet volume V_i as a function of *We* in both jetting and partial rebound regimes in Figure 15. We can identify three distinct regions in Figure 15 that correspond to the situations how satellite droplets are produced, including (I) jetting with relatively low-viscosity solution of ≤ 25%G (μ ≤ 2.3 mPa•s), (II) jetting with more viscous solution, and (III) partial rebound. The diameter of the rebounding droplet produced in the partial rebound is usually 10 or 100 times larger than that of the top droplet ejected in the jetting event. As a result, the volume ratio of the satellite droplet in Region III is significantly larger than that in other two regions. Figure 15 shows that V_s/V_i in Region III varies in a narrow range from 0.12 to 0.63, whereas V_s/V_i in Regions I and II varies by several orders of magnitude (i.e., from 10^{-2} to 10^{-7}). As the ejected satellite droplet in the jetting event gets smaller and faster with the increase in the impact velocity, V_s/V_i in Regions I and II generally decreases with increasing *We*. Overall, the experimental data for the jet droplets collapse into two scaling lines, which can be fitted by a power law $V_s/V_i \sim We^{\alpha}$, where the scaling exponent α depends on the viscosity. α = 4 in Region I for less viscous solutions ($\mu \leq 2.3$ mPa•s), whereas α = 11 in Region II for more viscous solutions.

For a given solution, the approximately constant size of the rebounding droplet regardless of the impact velocity is the result of the breakup of the elongated liquid column caused by the Rayleigh-Plateau instability. In all partial rebound cases, the maximum height H_{max} (as defined in Figure 14) of the thick liquid thread during retraction varies in a narrow range from 4.15 to 4.76 mm, and its diameter D_c varies from 0.96 to 1.26 mm. According to the Rayleigh-Plateau instability, a cylindrical jet becomes unstable and breaks up into droplets when the wavelength of disturbance along the jet shape is larger than the perimeter of the jet. Therefore, we hypothesize that the partial rebound occurs when the height of the liquid column exceeds its perimeter during retraction of the droplet, i.e., $H_{max} > \pi D_c$. To check this hypothesis, the normalized maximum height H_{max} / D_c is plotted as a function of *We* for all partial rebound cases in Figure 16(a). It is clear that H_{max} / D_c has a small variation from 3.81 to 4.53 and is larger than π for all cases. Therefore, the stretched liquid column in the recoil phase needs to grow tall enough to pinch off due to the Rayleigh-Plateau instability. Additionally, we find that in the partial rebound regime the time t_h for the stretched liquid column to reach H_{max} is approximately 12.8 to 15.6 ms after impact regardless of the impact velocity and fluid viscosity, suggesting the phenomenon is governed by the inertial-capillary flow. We now normalize t_h by the kinetic time $t_k = D_i/U_i$ and plot the normalized time $t_h U_i/D_i$ against *We* for all cases in Figure 16(b).We can clearly find that $t_h U_i/D_i$ obeys the power law of $t_h U_i/D_i \sim We^{0.5}$, which follows from the expectation that t_h scales with the capillary time, i.e., $t_h \sim (\rho D_i^3/\sigma)^{0.5}$. So, the partial rebound involves the higher harmonic capillary wave along the liquid surface.

4. Conclusion

Droplet impingement experiments are performed on a micro-pillared hydrophilic substrate. The dispensed droplet diameter is maintained at 2.7 mm in the experiments with impact velocities varying between 0.49 and 1.17 m/s. Water-glycerol mixtures are used primarily to vary viscosity between 0.96 mPa•s and 10.5 mPa•s. We have observed a range of impact phenomena such as spreading, high-speed jetting, and partial rebound. The regime map of impact outcomes constructed conveys the effects of impact velocity and viscosity on the impact dynamics at a glance. The high-speed jets observed during the recoil of the droplet are generated by the collapse of the air cavity formed in the center of the deformed droplet. For our microstructured partially wetting surface, the jets arise at 9.1 ≤ *We* ≤ 67.2. Within this range, the jet ejects one droplet at low *We* and multiple droplets at high *We*. Partial rebound only occurs for less viscous fluids of viscosity $\mu \leq 2.3$ mPa•s at relatively high Weber number in the range of 16.3 ≤ *We* ≤ 55.9. The size of the rebounding droplet ranges from hundreds of micrometers to around 1 mm.

The maximum spreading factor β_{max} in our experiments generally follows the scaling law of $\beta_{max} \sim We^{0.25}$, suggesting the spreading is in the capillary regime. However, β_{max} for the most viscous fluid 55%G (μ = 10.5 mPa•s) is shown to obey $\beta_{max} \sim We^{0.2}$. Our further analysis indicates that the viscous dissipation due to flow between the micropillars

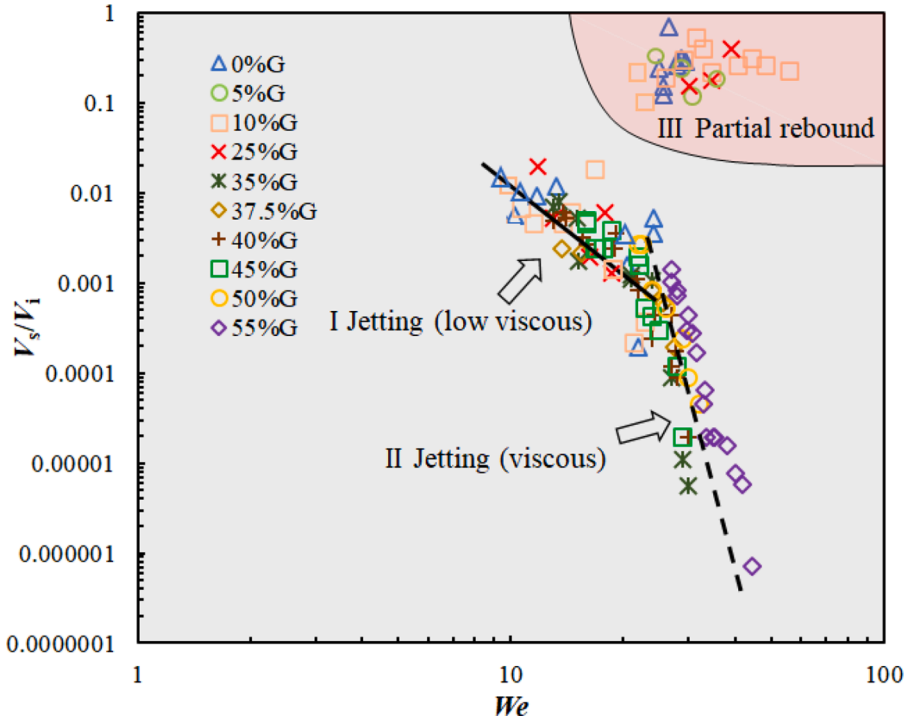

Figure 15. Volume ratio V_s/V_i of the satellite droplet to the initial droplet plotted against We for all solutions. The solid line and dashed line are the power fits with $V_s/V_i \sim We^{-4}$ and $V_s/V_i \sim We^{-4}$, respectively.

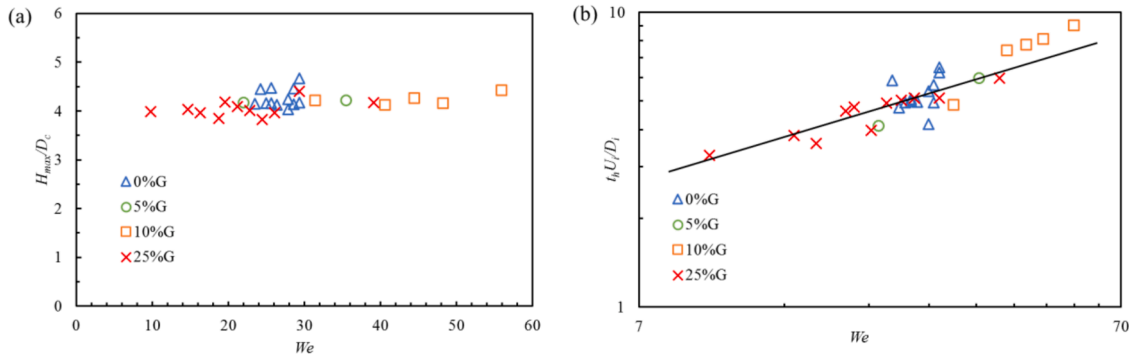

Figure 16. (a) the normalized maximum height H_{max} / D_c plotted as a function of We for all partial rebound cases; (b) the normalized time t_hU_i/D_i plotted as a function of We for all partial rebound cases with the solid line representing the power law of $t_hU_i/D_i \sim We^{1/2}$.

on the substrate becomes increasingly important for more viscous solutions. As a result, the scaling law of $\beta_{max} \sim We^{0.2}Re^{0.04}$ provides the best correlation for our experimental data of β_{max}. We also show that the dissipative energy E_d normalized by initial surface energy SE_i obeys the power law of $Ed/SE_i \sim We^{1.2}Re^{0.96}$.

We show that the profiles of the cavity-collapse driven jet at different times can collapse into one master curve after the profiles being scaled using the shape factor $r = (\sigma/\rho)^{1/3}(t\text{-}t_c)^{\alpha}$, suggesting that the jet exhibits self-similar growth over time. The pinch-off process of the jet is dominated by the capillary and inertial forces because the neck diameter n_d normalized by the capillary length l_c is found to reduce at the power law $n_d/l_c \sim \tau^{0.63}$. Our data also reveal that the relationship between the top jet droplet diameter and jet velocity obeys the scaling law of $R_d/l_\mu \sim V_j/V_\mu{}^{-5/3}$.

Lastly, we find that the size of rebounding satellite droplet in the partial rebound is not significantly influenced by the impact velocity. The volume ratio of the rebounding droplet to original droplet varies in a narrow range from 0.12 to 0.63 with respect to *We*, whereas the volume ratio of the satellite droplet produced in jetting phenomenon varies by several orders of magnitude. By analyzing the geometry of the inertially stretched thick liquid column prior to the breakup, we show that the breakup process of the liquid column is caused by the Rayleigh-Plateau instability. Additionally, the elapsed time between droplet impingement and partial rebound is found to follow the scaling relation $t_h \sim (\rho D_i^3/\sigma)^{0.5}$.

CRediT authorship contribution statement

Brooklyn Asai: Formal analysis, Methodology, Software, Investigation, Visualization, Writing – original draft. **Hua Tan:** Conceptualization, Data curation, Funding acquisition, Supervision, Resources, Project administration, Writing – review & editing. **Anayet Ullah Siddique:** Investigation, Visualization, Writing – original draft.

Declaration of Competing Interest

The authors declare that they have no known competing financial interests or personal relationships that could have appeared to influence the work reported in this paper.

Data Availability

Data will be made available on request.

ACKNOWLEDGEMENTS

The work is funded in part by National Science Foundation Grant CBET-1701339.

REFERENCES

Ahmad, D, van den Boogaert, I, Miller, J, Presswell, R, Jouhara, H, 2018. Hydrophilic and hydrophobic materials and their applications. Energy Sources, Part A: Recovery, Utilization, and Environmental Effects 40, 2686–2725. https://doi.org/10.1080/15567036.2018.1511642.

Baek, S, Yong, K, 2020. Impact dynamics on SLIPS: Effects of liquid droplet's surface tension and viscosity. Applied Surface Science 506, 144689. https://doi.org/10.1016/j.apsusc.2019.144689.

Bartolo, D, Josserand, C, Bonn, D, 2005. Retraction dynamics of aquous drops upon impact on nonwetting surfaces. Journal of Fluid Mechanics 545, 329. https://doi.org/10.1017/S0022112005007184.

Bartolo, D, Josserand, C, Bonn, D, 2006. Singular Jets and Bubbles in Drop Impact. Phys Rev Lett 96, 124501. https://doi.org/10.1103/PhysRevLett.96.124501.

Baxter, J, Mitragotri, S, 2006. Needle-free liquid jet injections: mechanisms and applications. Expert Rev Med Devices 3, 565–574. https://doi.org/10.1586/17434440.3.5.565.

Brasz, CF, Bartlett, CT, Walls, PLL, Flynn, EG, Yu, YE, Bird, JC, 2018. Minimum size for the top jet drop from a bursting bubble. Phys Rev Fluids 3, 074001. https://doi.org/10.1103/PhysRevFluids.3.074001.

Budakli, M, 2021. Prediction of maximum spreading factor after drop impact: Development of a novel semi-analytical model incorporating effect of surface roughness. Colloid and Interface Science Communications 41, 100384. https://doi.org/10.1016/j.colcom.2021.100384.

Chen, L, Li, L, Li, Z, Zhang, K, 2017. Submillimeter-Sized Bubble Entrapment and a High-Speed Jet Emission during Droplet Impact on Solid Surfaces. Langmuir 33, 7225–7230. https://doi.org/10.1021/acs.langmuir.7b01506.

Chubynsky, MV, Belousov, KI, Lockerby, DA, Sprittles, JE, 2020. Bouncing off the Walls: The Influence of Gas-Kinetic and van der Waals Effects in Drop Impact. Phys Rev Lett 124, 084501. https://doi.org/10.1103/PhysRevLett.124.084501.

Clanet, C, Béguin, C, Richard, D, Quéré, D, 2004. Maximal deformation of an impacting drop. Journal of Fluid Mechanics 517, 199–208. https://doi.org/10.1017/S0022112004000904.

Courbin, L, Bird, JC, Stone, HA, 2006. Splash and anti-splash: Observation and design. Chaos 16, 041102. https://doi.org/10.1063/1.2390551.

Deng, X, Huang, C, Liu, S, Yang, C, Wu, P, He, J, Jiang, W, 2021. Urea Melt Marbles Developed by Enwrapping Urea Melt Droplets with Superhydrophobic Particles: Preparation, Properties, and Application in Large Urea Granule Production. Advanced Materials Interfaces 8, 2100253. https://doi.org/10.1002/admi.202100253.

Ding, H, Li, EQ, Zhang, FH, Sui, Y, Spelt, PDM, Thoroddsen, ST, 2012. Propagation of capillary waves and ejection of small droplets in rapid droplet spreading. Journal of Fluid Mechanics 697, 92–114. https://doi.org/10.1017/jfm.2012.49.

Ding, S, Liu, X, Wu, X, Zhang, X, 2020. Droplet breakup and rebound during impact on small cylindrical superhydrophobic targets. Physics of Fluids 32, 102106. https://doi.org/10.1063/5.0024837.

Driessen, T, Jeurissen, R, Wijshoff, H, Toschi, F, Lohse, D, 2013. Stability of viscous long liquid filaments. Physics of Fluids 25, 062109. https://doi.org/10.1063/1.4811849.

Eggers, J, Villermaux, E, 2008. Physics of liquid jets. Rep Prog Phys 71, 036601. https://doi.org/10.1088/0034-4885/71/3/036601.

Fedorchenko, AI, Wang, A-B, Wang, Y-H, 2005. Effect of capillary and viscous forces on spreading of a liquid drop impinging on a solid surface. Physics of Fluids 17, 093104. https://doi.org/10.1063/1.2038367.

Gañán-Calvo, AM, 2017. Revision of Bubble Bursting: Universal Scaling Laws of Top Jet Drop Size and Speed. Phys Rev Lett 119, 204502. https://doi.org/10.1103/PhysRevLett.119.204502.

Gekle, S, Gordillo, JM, 2010. Generation and breakup of Worthington jets after cavity collapse. Part 1. Jet formation. Journal of Fluid Mechanics 663, 293–330. https://doi.org/10.1017/S0022112010003526.

Ghabache, E, Antkowiak, A, Josserand, C, Séon, T, 2014. On the physics of fizziness: How bubble bursting controls droplets ejection. Physics of Fluids 26, 121701. https://doi.org/10.1063/1.4902820.

Ghigliotti, G, Zhou, C, Feng, JJ, 2013. Simulations of the breakup of liquid filaments on a partially wetting solid substrate. Physics of Fluids 25, 072102. https://doi.org/10.1063/1.4812252.

Guo, J, Zou, S, Lin, S, Zhao, B, Deng, X, Chen, L, 2020. Oblique droplet impact on superhydrophobic surfaces: Jets and bubbles. Physics of Fluids 32, 122112. https://doi.org/10.1063/5.0033729.

Hao, J, Lu, J, Lee, L, Wu, Z, Hu, G, Floryan, JM, 2019. Droplet Splashing on an Inclined Surface. Phys Rev Lett 122, 054501. https://doi.org/10.1103/PhysRevLett.122.054501.

Kolinski, JM, Mahadevan, L, Rubinstein, SM, 2014. Drops can bounce from perfectly hydrophilic surfaces. EPL (Europhysics Letters) 108, 24001. https://doi.org/10.1209/0295-5075/108/24001.

Laan, N, de Bruin, KG, Bartolo, D, Josserand, C, Bonn, D, 2014. Maximum Diameter of Impacting Liquid Droplets. Phys Rev Applied 2, 044018. https://doi.org/10.1103/PhysRevApplied.2.044018.

Lai, C-Y, Eggers, J, Deike, L, 2018. Bubble Bursting: Universal Cavity and Jet Profiles. Phys Rev Lett 121, 144501. https://doi.org/10.1103/PhysRevLett.121.144501.

Lee, JB, et al., 2016. Universal rescaling of drop impact on smooth and rough surfaces. Journal of Fluid Mechanics 786. https://doi.org/10.1017/jfm.2015.620.

Lekshmi, BS, Yadav, AS, Ranganathan, P, Varanakkottu, SN, 2020. Simple and Continuous Fabrication of Janus Liquid Marbles with Tunable Particle Coverage Based on Controlled Droplet Impact. Langmuir 36, 15396–15402. https://doi.org/10.1021/acs.langmuir.0c02988.

Lhuissier, H, Villermaux, E, 2012. Bursting bubble aerosols. Journal of Fluid Mechanics 696, 5–44. https://doi.org/10.1017/jfm.2011.418.

Li, B, Lin, S, Wang, Y, Yuan, Q, Joo, SW, Chen, L, 2020. Promoting rebound of impinging viscoelastic droplets on heated superhydrophobic surfaces. New J Phys 22, 123001. https://doi.org/10.1088/1367-2630/abcacf.

Li, EQ, Langley, KR, Tian, YS, Hicks, PD, Thoroddsen, ST, 2017. Double Contact During Drop Impact on a Solid Under Reduced Air Pressure. Phys Rev Lett 119, 214502. https://doi.org/10.1103/PhysRevLett.119.214502.

Li, T, Zhang, AM, Wang, S-P, Li, S, Liu, W-T, 2019. Bubble interactions and bursting behaviors near a free surface. Physics of Fluids 31, 042104. https://doi.org/10.1063/1.5088528.

Li, X, Mao, L, Ma, X, 2013. Dynamic Behavior of Water Droplet Impact on Microtextured Surfaces: The Effect of Geometrical Parameters on Anisotropic Wetting and the Maximum Spreading Diameter. Langmuir 29, 1129–1138. https://doi.org/10.1021/la304567s.

Lin, S, Zhao, B, Zou, S, Guo, J, Wei, Z, Chen, L, 2018. Impact of viscous droplets on different wettable surfaces: Impact phenomena, the maximum spreading factor, spreading time and post-impact oscillation. Journal of Colloid and Interface Science 516, 86–97. https://doi.org/10.1016/j.jcis.2017.12.086.

Liu, Z, Pan, X, Ma, Q, Fang, H, 2020. Receding Dynamics of Droplet Deposition on a Smooth Surface from a Central Jet to Secondary Droplet Emission. Langmuir 36, 15082–15093. https://doi.org/10.1021/acs.langmuir.0c02643.

Lv, C, Hao, P, Zhang, X, He, F, 2016. Drop impact upon superhydrophobic surfaces with regular and hierarchical roughness. Appl Phys Lett 108, 141602. https://doi.org/10.1063/1.4945662.

Malla, LK, Patil, ND, Bhardwaj, R, Neild, A, 2017. Droplet Bouncing and Breakup during Impact on a Microgrooved Surface. Langmuir 33, 9620–9631. https://doi.org/10.1021/acs.langmuir.7b02183.

Mao, T, Kuhn, DCS, Tran, H, 1997. Spread and rebound of liquid droplets upon impact on flat surfaces. AIChE Journal 43, 2169–2179. https://doi.org/10.1002/aic.690430903.

Modak, CD, Kumar, A, Tripathy, A, Sen, P, 2020. Drop impact printing. Nat Commun 11, 4327. https://doi.org/10.1038/s41467-020-18103-6.

Nemani, SK, et al., 2018. Surface Modification of Polymers: Methods and Applications. Advanced Materials Interfaces 5, 1801247. https://doi.org/10.1002/admi.201801247.

Parihar, V, Chakraborty, S, Das, S, Chakraborty, S, DasGupta, S, 2021. Role of anisotropic pinning and liquid properties during partial rebound of droplets on unidirectionally structured hydrophobic surfaces. Chemical Engineering Science 230, 116197. https://doi.org/10.1016/j.ces.2020.116197.

Pasandideh-Fard, M, Qiao, YM, Chandra, S, Mostaghimi, J, 1996. Capillary effects during droplet impact on a solid surface. Physics of Fluids 8, 650–659. https://doi.org/10.1063/1.868850.

Prasad, GVVSV, Dhar, P, Samanta, D, 2022. Postponement of dynamic Leidenfrost phenomenon during droplet impact of surfactant solutions. International Journal of Heat and Mass Transfer 189, 122675. https://doi.org/10.1016/j.ijheatmasstransfer.2022.122675.

Rao, DCK, Karmakar, S, Basu, S, 2018. Bubble dynamics and atomization mechanisms in burning multi-component droplets. Physics of Fluids 30, 067101. https://doi.org/10.1063/1.5035384.

Rioboo, R, Tropea, C, Marengo, M, 2001. OUTCOMES FROM A DROP IMPACT ON SOLID SURFACES. Atomiz Spr 11, 12. https://doi.org/10.1615/AtomizSpr.v11.i2.40.

Roy, D, Pandey, K, Banik, M, Mukherjee, R, Basu, S, 2019. Dynamics of droplet impingement on bioinspired surface: insights into spreading, anomalous stickiness and break-up. Proceedings of the Royal Society A: Mathematical, Physical and Engineering Sciences 475, 20190260. https://doi.org/10.1098/rspa.2019.0260.

Siddique, AU, Trimble, M, Zhao, F, Weislogel, MM, Tan, H, 2020. Jet ejection following drop impact on micropillared hydrophilic substrates. Phys Rev Fluids 5, 063606. https://doi.org/10.1103/PhysRevFluids.5.063606.

Šikalo, Š, Wilhelm, HD, Roisman, IV, Jakirlić, S, Tropea, C, 2005. Dynamic contact angle of spreading droplets: Experiments and simulations. Physics of Fluids 17, 062103. https://doi.org/10.1063/1.1928828.

Tan, H, 2017. Numerical study on splashing of high-speed microdroplet impact on dry microstructured surfaces. Computers & Fluids 154, 142–166. https://doi.org/10.1016/j.compfluid.2017.05.014.

Thoroddsen, ST, Etoh, TG, Takehara, K, 2007a. Experiments on bubble pinch-off. Physics of Fluids 19, 042101. https://doi.org/10.1063/1.2710269.

Thoroddsen, ST, Etoh, TG, Takehara, K, 2007b. Microjetting from wave focusing on oscillating drops. Physics of Fluids 19, 052101. https://doi.org/10.1063/1.2718479.

Thoroddsen, ST, Etoh, TG, Takehara, K, 2008. High-Speed Imaging of Drops and Bubbles. Annual Review of Fluid Mechanics 40, 257–285. https://doi.org/10.1146/annurev.fluid.40.111406.102215.

Tsai, P, Pacheco, S, Pirat, C, Lefferts, L, Lohse, D, 2009. Drop Impact upon Micro- and Nanostructured Superhydrophobic Surfaces. Langmuir 25, 12293–12298. https://doi.org/10.1021/la900330q.

Ukiwe, C, Kwok, DY, 2005. On the Maximum Spreading Diameter of Impacting Droplets on Well-Prepared Solid Surfaces. Langmuir 21, 666–673. https://doi.org/10.1021/la0481288.

Versluis, M, 2013. High-speed imaging in fluids. Exp Fluids 54, 1458. https://doi.org/10.1007/s00348-013-1458-x.

Wang, F, Yang, L, Wang, L, Zhu, Y, Fang, T, 2019. Maximum Spread of Droplet Impacting onto Solid Surfaces with Different Wettabilities: Adopting a Rim–Lamella Shape. Langmuir 35, 3204–3214. https://doi.org/10.1021/acs.langmuir.8b03748.

Worthington, AM, 1909. A Study of Splashes Science 29, 464–465. https://doi.org/10.1126/science.29.742.464.

Yamamoto, K, Takezawa, H, Ogata, S, 2016. Droplet impact on textured surfaces composed of commercial stainless razor blades. Colloids and Surfaces A: Physicochemical and Engineering Aspects 506, 363–370. https://doi.org/10.1016/j.colsurfa.2016.06.024.

Yu, F, Lin, S, Yang, J, Fan, Y, Wang, D, Chen, L, Deng, X, 2020. Prompting Splash Impact on Superamphiphobic Surfaces by Imposing a Viscous Part. Advanced Science 7, 1902687. https://doi.org/10.1002/advs.201902687.

Yuan, Z, Matsumoto, M, Kurose, R, 2021. Directional rebounding of a droplet impinging hydrophobic surfaces with roughness gradients. International Journal of Multiphase Flow 138, 103611. https://doi.org/10.1016/j.ijmultiphaseflow.2021.103611.

Zeff, BW, Kleber, B, Fineberg, J, Lathrop, DP, 2000. Singularity dynamics in curvature collapse and jet eruption on a fluid surface. Nature 403, 401–404. https://doi.org/10.1038/35000151.

Zhang, H, et al., 2019. Dynamic behavior of water drops impacting on cylindrical superhydrophobic surfaces. Physics of Fluids 31, 032104. https://doi.org/10.1063/1.5083070.

Zhao, B, Wang, X, Zhang, K, Chen, L, Deng, X, 2017. Impact of Viscous Droplets on Superamphiphobic Surfaces. Langmuir 33, 144–151. https://doi.org/10.1021/acs.langmuir.6b03862.

Zhao, W, Lin, S, Chen, L, Li, EQ, Thoroddsen, ST, Thoraval, M-J, 2020. Jetting from an impacting drop containing a particle. Physics of Fluids 32, 011704. https://doi.org/10.1063/1.5139534.